Preprint version of Physics in Medicine and Biology vol. 59 issue 12, 2014

Image Artefact Propagation in Motion Estimation and Reconstruction in Interventional Cardiac C-arm CT

K Müller[1,2], A K Maier[1,2], C Schwemmer[1,2], G Lauritsch[3], S De Buck[4], J-Y Wielandts[4], J Hornegger[1,2] and R Fahrig[5]

[1]Pattern Recognition Lab, Department of Computer Science, Friedrich-Alexander-Universität Erlangen-Nürnberg, Martensstr. 3, D-91058 Erlangen, Germany
[2]Erlangen Graduate School in Advanced Optical Technologies (SAOT), Paul-Gordan-Str. 6, D-91052 Erlangen, Germany
[3]Siemens AG, Healthcare Sector, Siemensstr. 1, D-91301 Forchheim, Germany
[4]Department of Cardiovascular Sciences, University of Leuven, Herestraat 49, B-3000 Leuven, Belgium
[5]Department of Radiology, Stanford University, 1201 Welch Road, CA-94305 Stanford, USA

E-mail: kerstin.mueller@cs.fau.de

Abstract. The acquisition of data for cardiac imaging using a C-arm CT system requires several seconds and multiple heartbeats. Hence, incorporation of motion correction in the reconstruction step may improve the resulting image quality. Cardiac motion can be estimated by deformable 3-D/3-D registration performed on initial 3-D images of different heart phases. This motion information can be used for a motion-compensated reconstruction allowing the use of all acquired data for image reconstruction. However, the result of the registration procedure and hence the estimated deformations are influenced by the quality of the initial 3-D images. In this paper, the sensitivity of the 3-D/3-D registration step to the image quality of the initial images is studied. Different reconstruction algorithms are evaluated for a recently proposed cardiac C-arm CT acquisition protocol. The initial 3-D images are all based on retrospective electrocardiogram (ECG)-gated data. ECG-gating of data from a single C-arm rotation provides only a few projections per heart phase for image reconstruction. This view sparsity leads to prominent streak artefacts and a poor signal to noise ratio. Five different initial image reconstructions are evaluated: (1) cone beam filtered-backprojection (FDK), (2) cone beam filtered-backprojection and an additional bilateral filter (FFDK), (3) removal of the shadow of dense objects (catheter, pacing electrode, etc.) before reconstruction with a cone beam filtered-backprojection (cathFDK), (4) removal of the shadow of dense objects before reconstruction with a cone beam filtered-backprojection and a bilateral filter (cathFFDK). The last method (5) is an iterative few-view reconstruction (FV), the prior image constrained compressed sensing (PICCS) combined with the improved total variation (iTV) algorithm. All reconstructions are investigated with respect to the final motion-compensated reconstruction quality. The algorithms were tested on a mathematical phantom data set with and without a catheter and on two porcine models using qualitative and quantitative measures. The quantitative results of the phantom experiments show that if no dense object is present within the scan field of view, the quality of the FDK initial images is sufficient for motion estimation via 3-D/3-D registration. When a catheter or pacing electrode is present, the shadow of these objects needs to be removed before the initial image reconstruction. An additional bilateral filter shows no major improvement with respect to the final motion-compensated reconstruction quality. The results with respect to image quality of

the cathFDK, cathFFDK and FV images are comparable. As conclusion, in terms of computational complexity, the algorithm of choice is the cathFDK algorithm.

1. Introduction

1.1. Purpose of this Work

Today, an angiographic C-arm system is the workhorse imaging system in interventional cardiology laboratories. In addition to conventional 2-D fluoroscopy, there is the possibility to acquire a set of 2-D high-resolution X-ray images from various directions and to compute a 3-D image. In comparison to conventional CT imaging, the X-ray source and detector are mounted on a flexible C-arm. Usually, the C-arm acquires on the order of a few hundred projection images while performing a sweep around the patient over 200° degrees, with a sweep requiring between 3 to 20 seconds.

Three-dimensional C-arm CT images of the cardiac chambers would provide valuable information to the cardiologist within the catheter lab setting to guide minimally invasive procedures such as valve replacements or device implantations (Hetterich et al. 2010). For example, in John et al. (John et al. 2010), the 3-D reconstruction of the aortic root is used for guidance of a transcatheter aortic valve implantation (TAVI) by overlaying the 3-D reconstruction onto the fluoroscopic images during the deployment of the prosthesis and to measure critical anatomical parameters in 3-D image space. However, their approach reconstructs only the aortic root and cannot visualize the ventricular outflow tract (non-circular aortic annulus), which is also of clinical interest for TAVI procedures (Schultz et al. 2013). Up to now, for wall motion analysis, pre-operative three-dimensional echocardiographic volumes are used for cardiac resynchronization therapy (CRT) procedures in order to find the optimal lead position (Döring et al. 2013). Three-dimensional C-arm reconstructions of the cardiac chambers in various heart states, directly in the catheter lab would provide valuable information for the cardiologist, e.g., during the CRT procedure (Wielandts et al. 2014).

Due to the long acquisition time of several seconds, covering several heart beats, 3-D imaging of dynamic objects such as the heart is still an open and challenging problem. An electrocardiogram (ECG)-signal is recorded synchronously with the acquisition and a relative heart phase can be assigned to each projection. In order to improve temporal resolution, the reconstruction can be performed with the subset of the projections that lie inside a certain ECG window centred at the favoured heart phase (Desjardins & Kazerooni 2004). However, with one C-arm rotation, the available number of projections is insufficient for imaging of the heart chambers (Lauritsch et al. 2006). Streak artefacts hamper the use of the reconstructed volumes.

One possibility for motion estimation and compensation is to use all acquired projection data in combination with compensation for the cardiac motion in the reconstruction step (Müller, Schwemmer, Hornegger, Zheng, Wang, Lauritsch, Maier, Schultz & Fahrig 2013). The cardiac motion can be estimated by registration of initial 3-D volumes of each heart phase to one reference heart phase. The goal of this paper is to find a suitable reconstruction algorithm for the initial 3-D volumes that can provide image quality sufficient for a pre-selected 3-D/3-D registration.

1.2. State-of-the-Art

Cardiac motion estimation has already been extensively investigated for other imaging modalities, such as cardiac computed tomography (CT) (Isola et al. 2010, Cammin et al. 2011), ultrasound (US) (Ledesma-Carbayo et al. 2001) or cardiac magnetic

resonance (MR) imaging (Perperidis et al. 2005). One possible solution for motion estimation is geometric modelling of cardiac surfaces, e.g., as described by van Stevendaal et al. for cardiac CT imaging (van Stevendaal et al. 2008). However, in C-arm CT the quality of the images reconstructed from projection images belonging to a single cardiac phase is degraded compared to cardiac CT image reconstructions. Therefore, a surface-based approach for C-arm imaging of the left ventricle has been developed. In that approach, dynamic surface models were built by fitting an initial surface mesh to the standard FDK reconstruction using all projection images and adapting the surface mesh according to the 2-D projection images (Chen et al. 2011). Another possibility for estimation of the cardiac motion, is to use 3-D/3-D registration of initial single-heartphase images. The deformation between a reference heart phase and other heart phases is computed by various optimization routines. The individual algorithms differ in the used motion model, objective function, constraints and optimization techniques. An extensive overview of deformable medical imaging registration algorithms is given in Sotiras et al. (Sotiras et al. 2013).

In C-arm CT the reconstruction of initial single-phase images of sufficient good image quality at different heart phases with projection data acquired during one single C-arm sweep is still an unsolved problem. The reconstruction quality of the initial single-phase images is highly dependent on the choice of the acquisition protocol. In recent studies, an image acquisition using multiple sweeps of the C-arm has been used (Lauritsch et al. 2006, Prümmer et al. 2009). The number of gated projection images increases and few-view artefacts are avoided. Techniques of 3-D/3-D registration can be applied to estimate the cardiac motion. However, the longer imaging time results in a higher contrast burden, radiation dose, and a long breath-hold for the patient. Furthermore, only a subset of heart phases can be reconstructed. In recent studies, an image acquisition using multiple sweeps of the C-arm has been used (Lauritsch et al. 2006, Prümmer et al. 2009). The number of gated projection images increases and few-view artefacts are reduced. Techniques of 3-D/3-D registration can be applied to estimate the cardiac motion. However, the longer imaging time results in a higher contrast burden, increased radiation dose, and a long breath-hold for the patient. Furthermore, only a subset of heart phases can be reconstructed. More recently, constrained iterative methods, often denoted as compressed sensing (CS) methods have been proposed in the literature. These approaches try to compensate for the loss in the data measurements by the introduction of sparsity regularizations or a priori information in the reconstruction. One approach proposed for cardiac cone-beam CT, is prior image constrained compressed sensing (PICCS) (Chen et al. 2012, Thèriault-Lauzier et al. 2012). The results are quite promising, but the image quality can still be improved; the images appear visually smoother and some loss of spatial resolution may occur. Recently, Mory et al. published a method, which also takes into account the strong correlation between successive heart phases (Mory et al. 2014).

Since the acquisition time plays an important role in cardiac imaging, a new protocol for cardiac C-arm CT was presented by De Buck et al. (De Buck et al. 2013). It is a single sweep protocol with 10–15 s scan time, combined with electrical stimulation of the heart beat at moderate rates of 100–150 bpm. It provides the possibility to reconstruct several heart phases based on retrospective ECG-gating. The quality of the initial single-phase reconstructed images is still critical for this new approach. Here, the impact of image quality of the initial single-phase images on 3-D/3-D image registration and on motion-compensated reconstruction is investigated. Preliminary results have already been presented in Müller et al. (Müller, Schwemmer,

Lauritsch, Rohkohl, Maier, Heidbüchel, De Buck, Nuyens, Kyriakou, Köhler, Fahrig & Hornegger 2013).

2. Methods and Materials

In order to perform a motion-compensated reconstruction, initial images are reconstructed using five different approaches (Section 2.1). The generated initial volumes are then registered by a 3-D/3-D deformable registration approach to estimate the cardiac motion (Section 2.2). Finally, the motion-compensated reconstruction employing the created motion vector fields is performed (Section 2.3).

2.1. Initial 3-D Image Generation

2.1.1. ECG Gating. For a single sweep ECG-gated reconstruction, a weighting function $\lambda(i, \boldsymbol{s}_{\text{ga}}) : \mathbb{N} \times \mathbb{R}^2 \mapsto [0, 1]$ is introduced, that assigns to each image an impact weight on the reconstruction result in the FDK approach (Feldkamp et al. 1984). Single sweep means only one rotation of the C-arm around the patient. The heart phase is denoted with $\phi \in [0, 1]$ and the relative heart phase of the i-th projection image is given by $\phi(i)$. The gating function λ is parametrized by a vector $\boldsymbol{s}_{\text{ga}}\,(\phi_r, w)^T$ with the reference heart phase $\phi_r \in [0, 1]$, and the phase-width $w \in (0, 1]$. The gating function $\lambda(i, \boldsymbol{s}_{\text{ga}})$ returns then the gating weight. The weighting function is centred at a reference heart phase ϕ_r and has the shape of a rectangular window (Schäfer et al. 2006). In these experiments, we use a strict rectangular gating function of minimal width, i.e. only one view per heart cycle is considered to reduce the motion blur to a minimum. This is possible due to the specific cardiac acquisition protocol (De Buck et al. 2013). Several heart phases $k = 1, \ldots, K$ can be reconstructed. Every heart phase $\phi_k \in \{1, \ldots, K\}$ corresponds to a relative heart phase of $\phi \in [0, 1]$ between two successive R-peaks (Desjardins & Kazerooni 2004). Therefore, in our case the weighting function $\lambda(i, \boldsymbol{s}_{\text{ga}})$ is a binary function.

2.1.2. 3-D Image Reconstruction. All initial image reconstructions are based on the selected ECG-gated data as described in Subsection 2.1.1.

ECG-gated Filtered-Backprojection Volume Reconstruction (FDK): For this approach, the projections are ECG-gated as described in Section 2.1.1 and the volumes are reconstructed with a standard FDK reconstruction algorithm (Feldkamp et al. 1984). The volume $f_{\phi_k}(\boldsymbol{x}, \boldsymbol{s}_{\text{ga}})$ represents one heart phase from 1, ..., K.

The resulting ECG-gated FDK images are highly corrupted by noise and suffer from severe streak artefacts.

Filtered ECG-gated Filtered-Backprojection Volume Reconstruction (FFDK): The FDK volumes are additionally filtered by a 3-D bilateral filter (Tomasi 1998) to reduce the streak artefacts and eliminate noise. The edge-preserving bilateral filter can be applied due to the high contrast inside the heart chambers compared to the streak artefacts. Streak artefacts arise from residual cardiac motion after ECG-gating and from dense objects, e.g. catheters inside the field-of-view. The letter ones are of higher intensity values than the streaks from residual motion. The bilateral filter parameter σ_r defines the similarity in the intensity range of the values and σ_d the spatial closeness using Gaussian filters. In our experiments, the parameters of the filter were set to σ_r

= 100 HU, $\sigma_d = 1$ voxel and the filter kernel size was set to 5. If the acquisition scenario changes, the values also need to be adapted. However, after filtering, the volumes still exhibit streak artefacts, e.g. caused by catheters and electrodes.

ECG-gated Filtered-Backprojection Volume Reconstruction with Removed Catheter (cathFDK): Both approaches from the previous paragraphs suffer not only from noise and undersampling artefacts, but also from artefacts induced by high-density objects like the pigtail catheter or a pacing electrode. Therefore, these objects need to be removed from the 2-D projection images.

The high density objects (catheters and pacing electrodes) are identified in the ECG-gated volumes $f_{\phi_k}(\boldsymbol{x}, \boldsymbol{s}_{\mathrm{ga}})$ to generate binary 3-D mask volumes $m_{\phi_k}(\boldsymbol{x})$. The segmentation process is restricted to a user defined region of interest (ROI), denoted as $r(\boldsymbol{x})$. For segmentation, the slices of the volumes $f_{\phi_k}(\boldsymbol{x}, \boldsymbol{s}_{\mathrm{ga}})$ are filtered with a 2-D median filter of size 2×2 pixels to reduce noise in the reconstructed volumes. Afterwards, a thresholding operation is applied with a pre-set threshold entered by the user and the segmented pixels are dilated by a circular object with a radius of 1 pixel. Finally, the consistency of the catheter over the slices is automatically checked and completed if necessary. The resulting mask images $m_{\phi_k}(\boldsymbol{x})$ are forward projected into the 2-D projection images which belong to the corresponding heart phase. Due to its simplicity, a ray casting approach is used for forward projection. Here, the maximum intensity value is computed along the ray. The 2-D mask images combined with the log-transformed projection images p_w are used for catheter segmentation and interpolation. In this paper, a low-frequency-based object masking called Subtract-and-Shift (SaS) is used for the removal of the catheter in the 2-D projection images (Schwemmer et al. 2010). The algorithm makes use of the fact that many dense objects do not absorb all incident radiation. Therefore, some remaining anatomical structure is still available within the region overlaid by the object and should be used by an interpolation algorithm. However, in principle, also different approaches for dense object removal could be used (Prell et al. 2009, Psychogios et al. 2013).

The resulting interpolated images $p_{r,\phi_k}(\boldsymbol{u})$ are used for ECG-gated filtered-backprojection reconstruction to provide an image $c_{\phi_k}(\boldsymbol{x})$ without catheters and electrodes.

Filtered ECG-gated Filtered-Backprojection Volume Reconstruction with Removed Catheter (cathFFDK): The volumes from the previous paragraph still exhibit strong noise. Hence, an additional bilateral filter can be applied, c.f. FFDK.

Few-view Volume Reconstruction (FV): Images are reconstructed with an iterative few-view reconstruction algorithm that takes into account the sparse sampling condition. Here, the prior image constrained compressed sensing (PICCS) (Chen et al. 2008) combined with the improved total variation (iTV) (Ritschl et al. 2011) algorithm is used. An FDK reconstruction with data from a whole short-scan is used as prior volume for the PICCS reconstruction. The objective function is minimized in an alternating manner, i.e. the raw data constraint is minimized in a first step and in the second step the sparsity cost function is optimized. In order to ensure that the raw data cost function converges to the optimal value and simultaneously ensure that the sparsity constraint converges to a low value, the improved total variation (iTV) was introduced by Ritschl et al. (Ritschl et al. 2011). The weighting parameter α

for the PICCS algorithm was set to 0.5, which is the upper bound of the optimal range from 0.4–0.5 (Theriault-Lauzier et al. 2012). The relaxation parameter β for the iTV optimization was set to 0.8 and the iTV parameter ω to 0.8 as in the original paper (Ritschl et al. 2010). A number of 4 data consistency and 10 objective function iterations were set. The whole optimization scheme was stopped when the data error improvement in the subsequent iterations fell below 10 %. A gradient descent optimizer with an adaptive linesearch was used for minimization of the objective function. The resulting volumes have minor streak artefacts, but appear to have visually smoother edges than the standard non-gated FDK reconstruction. Therefore, the resulting volumes are not of satisfying image quality for clinical usage and used as initial images for an additional motion estimation step.

2.2. Cardiac Motion Field Estimation via 3-D/3-D Registration

In order to estimate the cardiac motion, one heart phase needs to be chosen as reference phase. The corresponding volume is called reference volume and all other volumes are registered pairwise to the reference volume. The deformable registration is based on a uniform cubic B-spline. A multi-resolution scheme of 4 levels is used with a sampling factor of 2 on each pyramid level. In each dimension a number of 16 control points are used at the highest image resolution. The negative normalized cross correlation (NCC) is used as the objective function and is minimized with an adaptive stochastic gradient descent optimizer. Empirical experiments showed that 500 iterations on each pyramid level are sufficient to result in a minimal objective function value. In this paper, a toolbox called `elastix` for non-rigid registration of medical images is used for the 3-D/3-D motion estimation (Klein et al. 2010). In order to constrain motion field estimation to a certain region of interest (ROI), a regional mask is defined. In this first implementation the mask volume is generated manually by the user by defining a rough 2 cm margin around the heart chambers in the standard FDK reconstruction.

2.3. Motion-compensated Reconstruction

For final motion-compensated image reconstruction, the estimated motion is integrated into the backprojection step of the FDK algorithm (Grangeat et al. 2002, Schäfer et al. 2006). The actual compensation is performed by shifting the voxel to be reconstructed according to the motion vector field.

The resulting motion-compensated volumes are denoted by the type of the initial ECG-gated volume reconstruction with added MC for motion-compensation (FDK-MC, FFDK-MC, FV-MC, cathFDK-MC and cathFFDK-MC).

3. Experiments and Evaluation Methods

3.1. Phantom Models

A ventricle dataset (Müller, Maier, Fischer, Bier, Lauritsch, Schwemmer, Fahrig & Hornegger 2013, Maier et al. 2012, Maier et al. 2013) of a similar design to the XCAT phantom (Segars et al. 2008) was simulated. It was assumed that all materials have the same spectral absorption behaviour as water. The density of the contrasted left ventricle bloodpool was set to 2.5 g/cm^3, the density of the myocardial wall to 1.5 g/cm^3 and the contrasted blood in the aorta to 2.0 g/cm^3 (available online (Müller

& Maier 2013)). Data was simulated monochromatically using a clinical protocol with the same parameters as for the porcine models which are presented in Section 3.2.

Additionally, a phantom dataset is simulated with a polychromatic X-ray spectrum. We simulated a source spectrum $E(b)$ with $b \in [1, 36]$ from 10 keV to 90 keV peak voltage, and a time current product of 2.5 mAs per X-ray pulse (available online (Müller & Maier 2013)). A catheter was placed spanning the aorta and the left ventricle. The deformation of the catheter was estimated from the deformation field of the heart, assuming no stiffness. The material of the catheter is similar to copper in order to induce severe streak artefacts in the reconstructions. The catheter, bones and the bone marrow, have the material properties according to the mass attenuation coefficients of the NIST X-Ray Table ‡. For all other structures it was assumed that they have the same absorption behaviour as water with different densities similar to the FORBILD phantom §. The density of the ventricular bloodpool, myocardium and aorta was the same as in the monochromatic simulations.

Poisson-distributed noise was added to the simulated projection stacks such that the noise characteristics of the reconstructed images fit to the clinical scan protocol at 2.5 mAs and 90 kVp. The standard deviation inside the reconstructed homogeneous LV resulted in ≈80 HU. As gold standard, static projection images were generated without noise.

3.2. Porcine Models

The methods were also applied to two experimental datasets of porcine models (p_1, p_2). Image acquisition was performed using an Artis zee system (Siemens AG, Healthcare Sector, Forchheim, Germany). The acquisition time was 14.5 s capturing 381 projection images with 30 f/s, and an angular increment of 0.52° during one C-arm sweep (De Buck et al. 2013). The isotropic pixel resolution was 0.31 mm/pixel (0.19 mm in isocenter) and the detector size 1240 × 960 pixel. The heart rate was stimulated through external heart pacing to 131 bpm. A total of 32 heart cycles are acquired resulting in a number of reconstructed heart phases $K = 12$. A volume of ≈ 140–200 ml contrast agent fluid was administered intravenously at a speed of 10 ml/s (p_1) and 7 ml/s (p_2) beginning 5 s (p_1) and 10 s (p_2) before the X-ray rotation was started. Image reconstruction was performed on an image volume of $(25.6\text{ cm})^3$ distributed on a 256^3 voxel grid.

3.3. Evaluation Methods

For the dynamic phantom data, the 3-D error and a quantitative 3-D image metric can be evaluated. In order to measure only the artefacts introduced by the heart motion, the non-gated FDK reconstruction using all projections of the static heart phantom of the same heart phase is used as gold standard. The error as well as the image quality metric were evaluated inside a region of interest (ROI) denoted as Ω around the ventricle. For the phantom with the catheter, a static phantom of the different heart phases was created without the catheter and used as gold standard. The region of the catheter is also excluded from the evaluation, in order to focus on motion artefacts. Let $\boldsymbol{y} = \{y_i \,|\, i = 1, 2, \ldots, N\}$ be the gold standard image and $\boldsymbol{x} = \{x_i \,|, i = 1, 2, \ldots, N\}$ the motion-compensated or initial reconstructed image, with i denoting the index of

‡ http://physics.nist.gov/PhysRefData/Xcom/html/xcom1.html
§ http://www.imp.uni-erlangen.de/phantoms/thorax/thorax.htm

each voxel and N the number of voxels in the volume. The relative root mean square error (rRMSE) was used to quantify the 3-D reconstruction error

$$\mathrm{rRMSE}_{\phi_k} = \sqrt{\frac{1}{|\Omega|}\sum_{v\in\Omega}(\frac{x_v - y_v}{y_v})^2}, \tag{1}$$

where $|\Omega|$ denotes the number of voxels inside the ROI. All results were averaged over the heart phases ϕ_k, resulting in the overall rRMSE.

Additionally, as a 3-D image quality metric the universal image quality index (UQI) was computed (Wang & Bovik 2002). The UQI ranges from -1 to 1, with 1 as the best overlap between both reconstructions. The UQI is defined as

$$\mathrm{UQI}_{\phi_k} = \frac{4\cdot\sigma_{xy}\cdot\overline{x}\cdot\overline{y}}{\left(\sigma_x^2+\sigma_y^2\right)\left[(\overline{x})^2+(\overline{y})^2\right]}, \tag{2}$$

where $\overline{x}$, $\overline{y}$ represent the mean values, σ_x^2, σ_y^2 the variances, and

$$\sigma_{xy} = \frac{1}{|\Omega|-1}\sum_{v\in\Omega}(x_i-\overline{x})(y_i-\overline{y}). \tag{3}$$

All results were averaged over the heart phases, resulting in the overall UQI.

The motion-compensated reconstruction improves the sharpness of the edges. For analysis of edge profiles the start and end points $x_{i,1}$ and $x_{i,2}$ at the lateral wall of the ventricle are determined in the gold standard reconstruction and used for all other images. The slope $m_{i,\mathrm{GS}}$ is computed between these two points

$$m_{i,\mathrm{GS}} = \frac{\Delta y}{\Delta x} = \frac{y_{i,2}-y_{i,1}}{x_{i,2}-x_{i,1}}. \tag{4}$$

For the motion-compensated reconstructions, also the slope m_i between the given two points $x_{i,1}$, $x_{i,2}$ is determined. Consequently, the deviation δ_i between the slopes m_i and the $m_{i,\mathrm{GS}}$ can be computed by

$$\delta_i = \frac{|m_{i,\mathrm{GS}} - m_i|}{|m_{i,\mathrm{GS}}|}, \tag{5}$$

$$\Delta = \frac{1}{L}\sum_{i=1}^{L}\delta_i, \tag{6}$$

where L denotes the number of lines. In order to stabilize the result, and to eliminate small outliers, several lines are taken and the deviation δ_i is measured individually for each line. Afterwards the edge sharpness deviation δ_i for each line is averaged to determine the mean edge sharpness deviation Δ. Furthermore, in order to exclude outliers, the median is also quoted as Q_Δ. For the phantom data it is also possible to measure the accuracy and trend of the edge between each motion-compensated reconstruction and the gold standard. This is done by appropriately modifying Equation 1. The mean error τ of the trend of the edge profile and the median (Q_τ) is computed.

4. Results and Discussion

4.1. Phantom Data

4.1.1. Visual Inspection. The results of the phantom data without the catheter are presented in Fig. 1. The gold standard at a heart phase of about 30% is illustrated in

Fig. 1a. The non-gated FDK reconstruction has motion blur around the left ventricle and the myocardial wall is hardly visible (Fig. 1b). In Fig. 1c, the gated FDK depicts the myocardial wall, but is severely degraded by noise and streak artefacts. The FFDK and FV have less streak artefact and a lower noise level, but have a smoother image impression (Fig. 1d and 1e). Motion compensation almost eliminates streak artefacts and further reduces the noise level (Fig. 1f, 1g and 1h). All three motion-compensated reconstructions show comparable and good delineation of the left ventricle (Fig. 1f, 1g and 1h). Almost no difference can be seen when using different initial images (Fig. 1i, 1j and 1k).

For the phantom dataset with the simulated catheter the results are shown in Fig. 2 for a heart phase of about 30 %. The catheter causes severe streak artefacts in the ECG-gated reconstruction (Fig. 2c). The streaks are still present after bilateral filtering in Fig. 2d. Motion compensation does not eliminate these streak artefacts since the motion estimation is disturbed by them (Fig. 2h and 2i). Some initial images are less sensitive to the catheter. The FV, cathFDK and cathFFDK (Fig. 2e, 2f and 2g) show less streak artefact and consequently the corresponding motion compensated images show a much better image quality (Fig. 2j, 2k and 2l). The results of the FDK-MC and FFDK-MC reconstruction however, suffer from streak artefacts induced by the catheter (Fig. 2h and 2i). The cathFDK-MC, cathFFDK-MC and FV-MC show comparable results.

4.1.2. 3-D Image Metric. The results of the monochromatic phantom without the catheter at the $K = 12$ different relative heart phases are given in Table 1. All three motion-compensated reconstructions achieve comparable results, and the image quality improved with respect to the initial images.

For the phantom dataset with the simulated catheter, the results of the rRMSE and the UQI are given in Table 2. In the table only the quality values between the five different motion-compensated reconstructions are illustrated, since the visual appearance of the initial images is not of sufficient quality, see Fig. 2. The FDK-MC and the FFDK-MC have a higher rRMSE value compared to the FV-MC, cathFDK-MC and cathFFDK-MC, due to the fact that some streak artefacts are registered onto each other and result in streak artefacts in the final motion-compensated reconstruction. The same can be seen for the UQI values. The best result was achieved by the cathFDK-MC, only slightly inferior results are given by the cathFFDK-MC and the FV-MC.

4.1.3. Edge Response Profiles. Table 3 shows the results for the mean edge sharpness deviation Δ measurements of the phantom with the catheter. The reference lines and the mean edge profile is given in Fig. 3. The best result is given by the FV-MC approach and the cathFDK-MC. However the smallest error τ, measuring the trend of the edge profile, is seen for cathFDK-MC, resulting in edges very similar to the gold standard (Table 4). It is again visible that the FDK-MC and the FFDK-MC approach have slightly divergent sharpness compared to the gold standard due to the streak artefacts inside the reconstructions. These artefacts cause outliers in the line profiles and a higher standard deviation in the sharpness measurements. The cathFFDK-MC shows no improvement compared to the non-filtered version of cathFDK-MC, which may be due to the smoothing out of small structure of the myocardium in the initial images which cannot be recovered in the motion-compensated reconstruction. Overall,

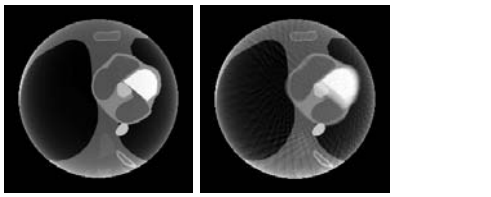

(a) Non-gated FDK result of static phantom.

(b) Non-gated FDK result of dynamic phantom.

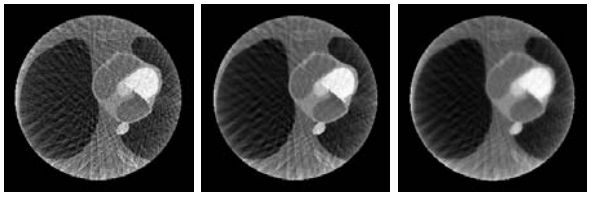

(c) FDK (d) FFDK (e) FV

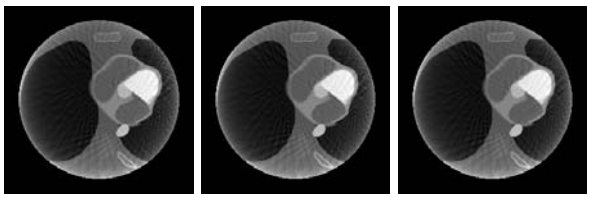

(f) FDK-MC (g) FFDK-MC (h) FV-MC

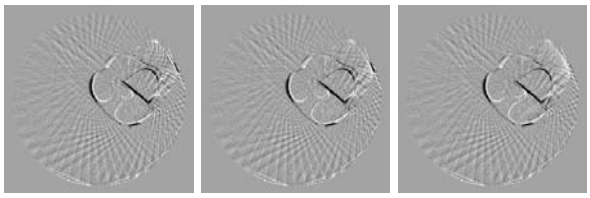

(i) Difference image between (c) and (f).

(j) Difference image between (d) and (g).

(k) Difference image between (e) and (h).

Figure 1: Central slice of initial volumes and motion-compensated reconstructions of the phantom model without any catheter and a relative heart phase of about 30 % (W 3100 HU, C 780 HU, slice thickness 1 mm).

the cathFDK-MC, cathFFDK-MC and the FV-MC differ only slightly when looking at all quantitative results.

4.2. Clinical Data

4.2.1. Visual Inspection. The results of the porcine data p_1 at a heart phase of about 30 % illustrate that the non-gated FDK reconstruction averages over all heart phases, as highlighted by the doubled catheter and blurred endocardium edges (Fig. 4a).

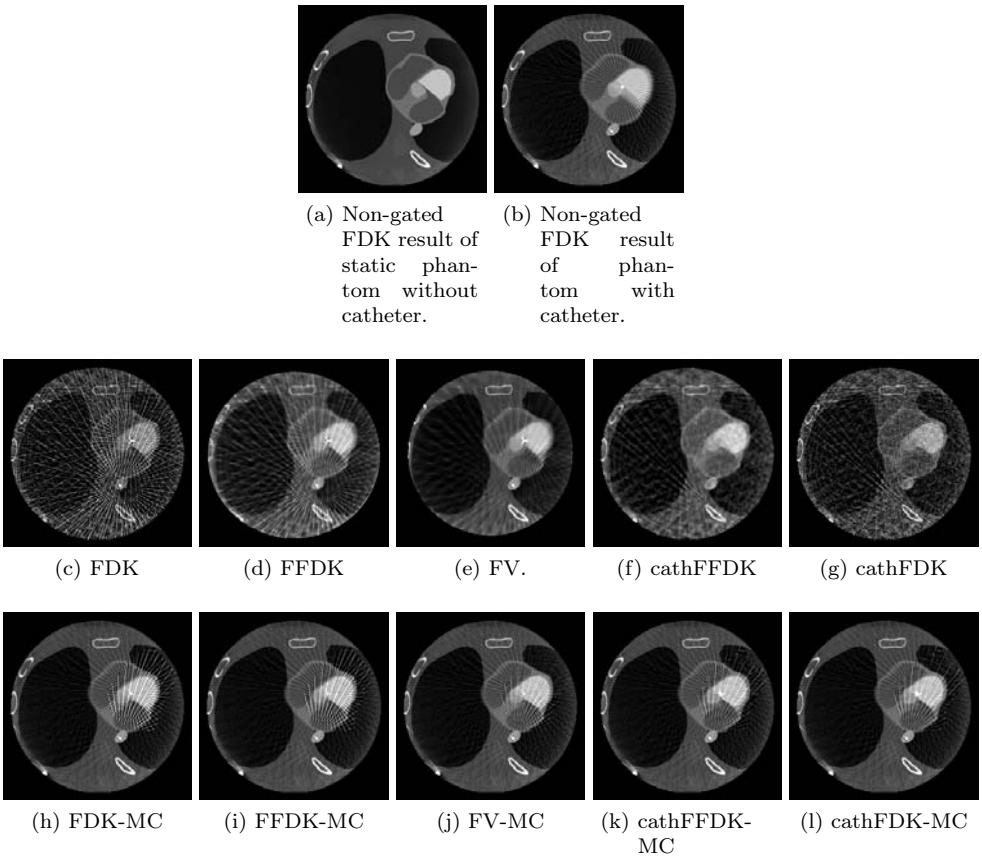

(a) Non-gated FDK result of static phantom without catheter.

(b) Non-gated FDK result of phantom with catheter.

(c) FDK (d) FFDK (e) FV. (f) cathFFDK (g) cathFDK

(h) FDK-MC (i) FFDK-MC (j) FV-MC (k) cathFFDK-MC (l) cathFDK-MC

Figure 2: Central slice of initial volumes and motion-compensated reconstructions of the phantom model with a catheter and a relative heart phase of about 30 % (W 3100 HU, C 780 HU, slice thickness 1 mm). The lateral myocardial wall can be precisely reconstructed in Fig. 2j, 2k and 2l.

Table 1: The rRMSE and UQI of the dynamic phantom model without a catheter for all $K = 12$ heart phases as mean and standard deviation. The best values are marked in bold.

Method	rRMSE	UQI
FDK-MC	0.09 ± 0.02	**0.98 ± 0.01**
FFDK-MC	**0.08 ± 0.02**	**0.98 ± 0.01**
FV-MC	**0.08 ± 0.02**	**0.98 ± 0.01**
FDK	0.14 ± 0.01	0.95 ± 0.01
FFDK	0.10 ± 0.02	0.97 ± 0.01
FV	0.10 ± 0.01	0.97 ± 0.01
Non-gated FDK	0.12 ± 0.04	0.96 ± 0.01

Table 2: The rRMSE and UQI of the dynamic phantom model with a catheter for all $K = 12$ heart phases as mean and standard deviation. The best values are marked in bold.

Method	rRMSE	UQI
FDK-MC	0.85 ± 0.34	0.84 ± 0.01
FFDK-MC	0.84 ± 0.33	0.87 ± 0.01
FV-MC	0.63 ± 0.28	0.93 ± 0.01
cathFDK-MC	**0.62 ± 0.43**	**0.94 ± 0.01**
cathFFDK-MC	0.63 ± 0.37	0.93 ± 0.01

Table 3: The mean edge sharpness deviation Δ and the median Q_Δ compared to the gold standard of the dynamic phantom model with a catheter for heart phases $\phi_3 \approx 30\,\%$ and $\phi_9 \approx 80\,\%$. The best values are marked in bold.

Method	Δ_{ϕ_3}	$Q_{\Delta_{\phi_3}}$	Δ_{ϕ_9}	$Q_{\Delta_{\phi_9}}$
FDK-MC	0.20 ± 0.12	0.19	0.34 ± 0.16	0.32
FFDK-MC	0.14 ± 0.10	0.15	0.18 ± 0.14	0.21
FV-MC	**0.11 ± 0.07**	**0.07**	0.11 ± 0.07	0.10
cathFDK-MC	0.14 ± 0.05	0.16	**0.07 ± 0.05**	**0.07**
cathFFDK-MC	0.15 ± 0.13	0.11	0.09 ± 0.06	0.09

Table 4: The mean τ and the median Q_τ of the accuracy of the edge profile compared to the gold standard of the dynamic phantom model with a catheter for heart phases $\phi_3 \approx 30\,\%$ and $\phi_9 \approx 80\,\%$. The best values are marked in bold.

Method	rRMSE_{ϕ_3}	$Q_{\tau_{\phi_3}}$	rRMSE_{ϕ_9}	$Q_{\tau_{\phi_9}}$
FDK-MC	0.47 ± 0.20	0.44	0.59 ± 0.18	0.63
FFDK-MC	0.39 ± 0.13	0.38	0.48 ± 0.14	0.52
FV-MC	0.28 ± 0.15	**0.21**	0.28 ± 0.06	0.28
cathFDK-MC	**0.26 ± 0.15**	0.25	**0.25 ± 0.04**	**0.24**
cathFFDK-MC	0.27 ± 0.17	0.26	0.28 ± 0.10	0.28

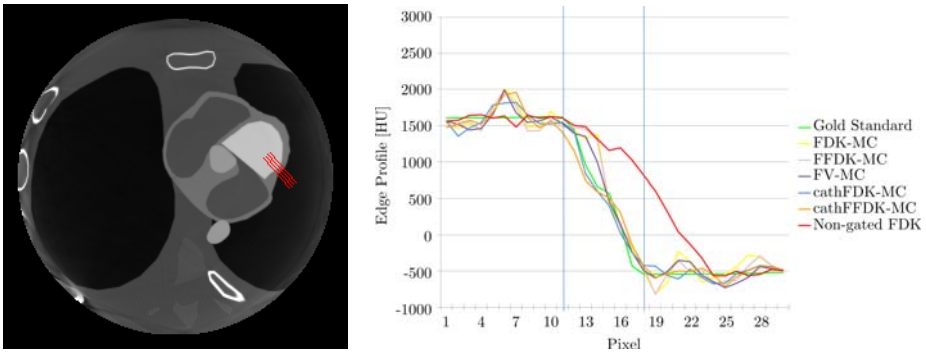

(a) Visualized lines for edge response function and sharpness for the catheter phantom.

(b) Mean edge response profile for phantom dataset with catheter of the different motion compensation algorithms at 30 % heart phase.

Figure 3: Measurements of the edge response profile for the catheter phantom.

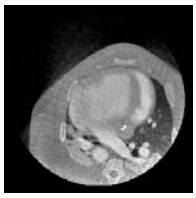

(a) Non-gated FDK reconstruction.

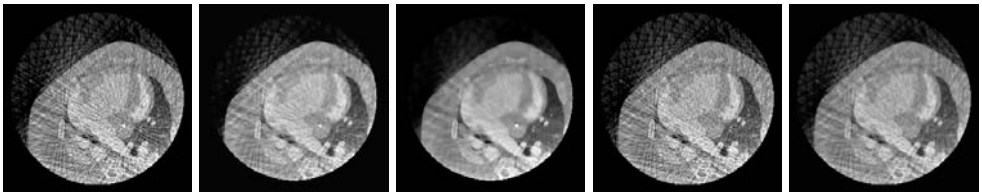

(b) FDK (c) FFDK (d) FV (e) cathFDK (f) cathFFDK

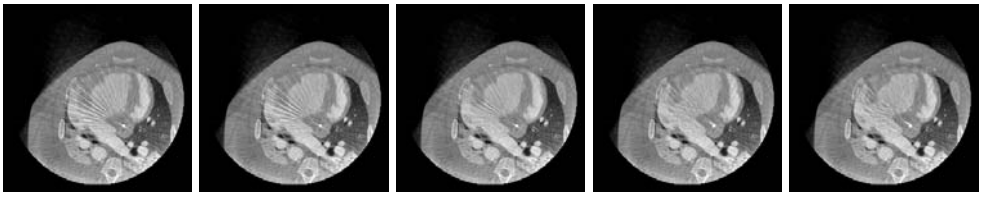

(g) FDK-MC (h) FFDK-MC (i) FV-MC (j) cathFDK-MC (k) cathFFDK-MC

Figure 4: Axial central slice of initial volumes, motion-compensated reconstructions of porcine model p_1 and a relative heart phase of about 30 % (W 2400 HU, C 226 HU, slice thickness 1 mm).

The gated FDK displays the sharp contours of the endocardium, however prominent streak artefacts are apparent (Fig. 4b). A better result is provided by the FFDK and FV reconstruction (Fig. 4c and 4d). However, both exhibit blurred streak artefacts and are severely smoothed. Looking at the cathFDK reconstruction (Fig. 4e), the artefacts from the catheter are removed, but the noise is still present in the volume. The noise is reduced in the cathFFDK volume in Fig. 4f. The motion-compensated reconstructions yield improved results (Fig. 4g, 4h, 4i, 4j and 4k). Overall, there is not much difference in image quality for the FV-MC, the cathFDK-MC and the cathFFDK-MC. The intensity of the remaining streak artefacts varies slightly.

Similar results can be observed for the porcine data p_2 at a heart phase of about 20 % illustrated in Figure 5.

4.2.2. Edge Response Profiles. For the analysis of the edge response profile of the porcine models (p_1, p_2) a similar sharpness measure as for the catheter phantom is used. However, no gold standard edge is known. Therefore, again a line profile is computed along a reference line i for each motion-compensated reconstruction. Each line is filtered with a Gaussian kernel in order to remove small outliers. In the filtered line profile the beginning $x_{i,1}$ and the end $x_{i,2}$ of the edge are determined. The

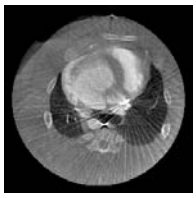

(a) Non-gated FDK reconstruction.

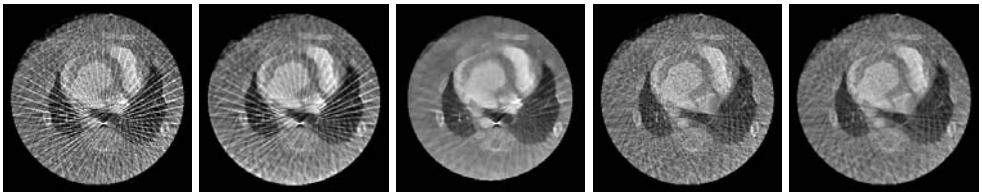

(b) FDK (c) FFDK (d) FV (e) cathFDK (f) cathFFDK

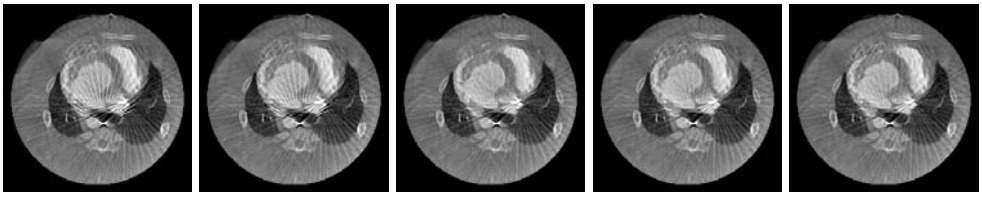

(g) FDK-MC (h) FFDK-MC (i) FV-MC (j) cathFDK-MC (k) cathFFDK-MC

Figure 5: Axial slice 28mm from the central slice of initial volumes, motion-compensated reconstructions of porcine model p_2 and a relative heart phase of about 20 % (W 2400 HU, C 226 HU, slice thickness 1 mm).

resulting slope m_i between these two points $x_{i,1}$, $x_{i,2}$ is computed, but the values from the non-filtered line are used. In order to stabilize the result, and to eliminate small outliers, several lines are taken and the m_i is measured individually for each line. Afterwards the edge sharpness m_i for each line is averaged to determine the mean edge sharpness Λ. Furthermore, in order to exclude outliers, the median Q_Λ is also provided. An example of the reference lines and the resulting mean edge profile is illustrated in Fig. 6. In Table 5, the results for the sharpness measures are given for the clinical data. The cathFFDK-MC has the steepest edge, however the cathFDK-MC also has a well delineated edge profile and differs only slightly. The FDK-MC and the FFDK-MC deviate for both datasets due to the different magnitude of streaking artefacts, present due to the catheter and pacing electrode. The FV-MC exhibits a high variation between the two porcine models and produces no reliable results.

4.3. Limitations and Challenges

3-D image reconstruction of large objects with medium contrast typically requires 20-30 projection images as input data. Only one projection image per heart cycle can be used for the reconstruction of each heart phase. Thus image acquisition lasts 20-30 heart cycles. Acquisition time has to be shortened in order to achieve a clinically

Table 5: The mean edge sharpness Λ and the median Q_Λ of the dynamic phantom model p_1 and p_2 for the heart phase $\phi_3 \approx 30\,\%$. The best values are marked in bold.

	p_1		p_2	
Method	Λ_{ϕ_3}	$Q_{\Lambda_{\phi_3}}$	Λ_{ϕ_3}	$Q_{\Lambda_{\phi_3}}$
FDK-MC	24.18 ± 7.02	23.85	42.20 ± 9.42	42.64
FFDK-MC	24.33 ± 2.15	24.12	45.46 ± 11.9	39.52
FV-MC	22.44 ± 4.76	21.20	48.44 ± 4.58	47.73
cathFDK-MC	25.04 ± 8.21	27.57	47.82 ± 3.95	**48.52**
cathFFDK-MC	**26.60 ± 7.26**	**28.55**	**49.45 ± 5.26**	47.69

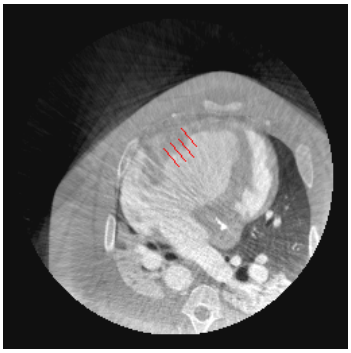

(a) Visualized lines for edge response function and sharpness for the porcine model p_1.

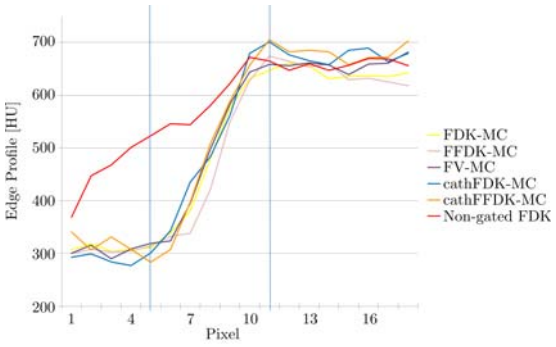

(b) Mean edge response profile for porcine dataset p_1 of the different motion compensation algorithms at 30% heart phase.

Figure 6: Measurements of the edge response profile for the porcine model p_1.

feasible protocol with respect to breath-hold and contrast dose. Moderate pacing is used for acceleration. Therefore, a pacing electrode is always in the field of view, which requires the virtual removal of its degrading shadow from the projection image. But, pacing also offers the advantage of having a stable heart rythm, and hence, a reliable selection of phase images. In the academic case that no dense object is inside the field of view, the FDK-MC, FFDK-MC and FV-MC achieved equally good image quality. Considering these three options, the computational complexity of FDK-MC is lowest. The robustness of the proposed algorithm with respect to the number of projections used for the initial image reconstruction needs to be evaluated in future experiments. Quite recently a reconstruction approach using significantly fewer projection images has been published (Mory et al. 2014). A different motion estimation strategy is applied there. A study comparing this new method to our approach would require a new study design and is beyond the scope of this paper.

5. Summary and Conclusion

For cardiac image acquisition with a C-arm CT, it is possible to compensate for the cardiac motion in the reconstruction step. We have presented cardiac motion estimation from initial 3-D volume data sets with a deformable B-spline registration. In the absence of dense objects like a catheter or pacing electrode the initial image quality of simple ECG-gated volumes is sufficient for motion estimation by 3-D/3-D

registration. If a dense object is present inside the scan field of view, the undersampled ECG-gated initial images suffer from streak artefacts which disturb the motion estimation. The shadow of the dense object has to be removed from the 2-D projection images as a preprocessing step before the reconstruction of the initial images. Using these volumes, motion is estimated with reasonable accuracy, hence no further image enhancement and processing is needed. The removal technique outperforms a particular iterative few-view reconstruction technique when comparing complexity and final image quality.

Disclaimer The concepts and information presented in this paper are based on research and are not commercially available.

Acknowledgments

The authors also gratefully acknowledge funding support from the NIH grant R01 HL087917 and of the Erlangen Graduate School in Advanced Optical Technologies (SAOT) by the German Research Foundation (DFG) in the framework of the German excellence initiative.

References

Cammin J, Khurd P, Kamen A, Tang Q, Kirchberg K, Chefd Hotel C, Bruder H & Taguchi K 2011 Combined motion estimation and motion compensated FBP for cardiac CT *in* M Kachelriess & M Rafecas, eds, '11th International Meeting on Fully Three-Dimensional Image Reconstruction in Radiology and Nuclear Medicine (Fully3D)' pp. 136–139.

Chen G H, Tang J & Leng S 2008 Prior image constrained compressed sensing (PICCS): A method to accurately reconstruct dynamic CT images from highly undersampled projection data sets *Med Phys* **35**(2), 660–663.

Chen G H, Thèriault-Lauzier P, Tang J, Nett B, Leng S, Zambelli J, Zhihua Q, Bevins N, Raval A & Reeder S 2012 Time-resolved interventional cardiac C-arm cone-beam CT: An application of the PICCS algorithm *IEEE Trans Med Imaging* **31**(4), 907–923.

Chen M, Zheng Y, Müller K, Rohkohl C, Lauritsch G, Boese J, Funka-Lea G, Hornegger J & Comaniciu D 2011 Automatic extraction of 3D dynamic left ventricle model from 2D rotational angiocardiogram *in* G Fichtinger, A Martel & T Peters, eds, 'Proceedings of the Medical Imaging and Computer Assisted Interventions (MICCAI) 2011' Vol. 6893 of *Lecture Notes in Computer Science* Springer Verlag Berlin Heidelberg pp. 471–478.

De Buck S, Dauwe D, Wielandts J Y, Claus P, Koehler C, Kyriakous Y, Janssens S, Heidbuchel H & Nuyens D 2013 A new approach for prospectively gated cardiac rotational angiography *in* R Nishikawa & B Whiting, eds, 'Proceedings of SPIE Medical Imaging 2013: Physics of Medical Imaging' Vol. 8668 p. 86682W.

Desjardins B & Kazerooni E 2004 ECG-gated cardiac CT *Am J Roentgenol* **182**(4), 993–1010.

Döring M, Braunschweig F, Eitel C, Gaspar T, Wetzel U, Nitsche B, Hindricks G & Piorkowski C 2013 Individually tailored left ventricular lead placement: lessons from multimodality integration between three-dimensional echocardiography and coronary sinus angiogram *Europace* **15**(5), 718–727.

Feldkamp L, Davis L & Kress J 1984 Practical cone-beam algorithm *J Opt Soc Am A* **1**(6), 612–619.

Grangeat P, Koenig A, Rodet T & Bonnet S 2002 Theoretical framework for dynamic cone-beam reconstruction algorithm based on a dynamic particle model *Phys Med Biol* **47**(15), 2611–2625.

Hetterich H, Redel T, Lauritsch G, Rohkohl C & Rieber J 2010 New x-ray imaging modalities and their integration with intravascular imaging and interventions *Int J Cardiovasc Imaging* **26**(7), 797–808.

Isola A, Grass M & Niessen W 2010 Fully automatic nonrigid registration-based local motion estimation for motion-corrected iterative cardiac CT reconstruction *Med Phys* **37**(3), 1093–1109.

John M, Liao R, Zheng Y, Nöttling A, Boese J, Kirschstein U, Kempfert J & Walther T 2010 System to guide transcatheter aortic valve implantations based on interventional c-arm ct imaging *in* T Jiang, N Navab, J Pluim & M Viergever, eds, 'Proceedings of the Medical Imaging and Computer Assisted Interventions (MICCAI) 2010' Vol. 6361 of *Lecture Notes in Computer Science* Springer Verlag Berlin Heidelberg pp. 375–382.

Klein S, Staring M, Murphy K, Viergever M & Pluim J 2010 elastix: a toolbox for intensity based medical image registration *IEEE Trans Med Imaging* **29**(2010), 196–205.

Lauritsch G, Boese J, Wigström L, Kemeth H & Fahrig R 2006 Towards cardiac C-arm computed tomography *IEEE Trans Med Imaging* **25**(7), 922–934.

Ledesma-Carbayo M, Kybic J, Desco M, Santos A & Unser M 2001 Cardiac motion analysis from ultrasound sequences using non-rigid registration *in* W Niessen & M Viergever, eds, 'Proceedings of the Medical Imaging and Computer Assisted Interventions (MICCAI) 2001' Vol. 2208 of *Lecture Notes in Computer Science* Springer Verlag pp. 889–896.

Maier A, Hofmann H, Berger M, Fischer P, Schwemmer C, Wu H, Müller K, Hornegger J, Choi J H, Riess C, Keil A & Fahrig R 2013 Conrad - a software framework for cone-beam imaging in radiology *Med Phys* **40**(11), 111914–1–8.

Maier A, Hofmann H, Schwemmer C, Hornegger J, Keil A & Fahrig R 2012 Fast simulation of X-ray projections of spline-based surfaces using an append buffer *Phys Med Biol* **57**(19), 6193–6210.

Müller K, Maier A, Fischer P, Bier B, Lauritsch G, Schwemmer C, Fahrig R & Hornegger J 2013 Left ventricular heart phantom for wall motion analysis *in* 'Proceedings of the IEEE Nuclear Science Symposium and Medical Imaging Conference (NSS/MIC) 2013'.

Müller K & Maier K 2013 'Cardiac Phantoms generated with Conrad'. `https://conrad.stanford.edu/data/heart`

Müller K, Schwemmer C, Hornegger J, Zheng Y, Wang Y, Lauritsch G, Maier A, Schultz C & Fahrig R 2013 Evaluation of interpolation methods for surface-based motion compensated tomographic reconstruction for cardiac angiographic C-arm data *Med Phys* **40**(3), 031107–1 –12.

Müller K, Schwemmer C, Lauritsch G, Rohkohl C, Maier A, Heidbüchel H, De Buck S, Nuyens D, Kyriakou Y, Köhler C, Fahrig R & Hornegger J 2013 Image artifact influence on motion compensated tomographic reconstruction in cardiac C-arm CT *in* R Leahy & J Qi, eds, 'Proceedings of the 12th International Meeting on Fully Three-Dimensional Image Reconstruction in Radiology and Nuclear Medicine (Fully3D)' pp. 98–101.

Mory C, Auvray V, Zhang B, Grass M, Schäfer D, Chen S, Carroll J, Rit S, Peyrin F, Douek P & Boussel L 2014 Cardiac c-arm computed tomography using a 3d + time roi reconstruction method with spatial and temporal regularization *Med Phys* **41**(2), 0219031–12.

Perperidis D, Mohiaddin R & Rueckert D 2005 Spatio-temporal free-form registration of cardiac MR image sequences *Med Image Anal* **9**(5), 441–456.

Prell D, Kyriakou Y, Struffert T, Dörfler A & Kalender W 2009 Metal artifact reduction for clipping and coiling in interventional c-arm ct *American Journal of Neuroradiology* **31**(4), 634–639.

Prümmer M, Hornegger J, Lauritsch G, Wigström L, Girard-Hughes E & Fahrig R 2009 Cardiac C-Arm CT: A unified framework for motion estimation and dynamic CT *IEEE Trans Med Imaging* **28**(11), 1836–1849.

Psychogios M N, Scholz B, Rohkohl C, Kyriakou Y, Mohr A, Schramm P, Wachter D, Wasser K & Knauth M 2013 Impact of a new metal artefact reduction algorithm in the noninvasive follow-up of intracranial clips, coils, and stents with flat-panel angiographic CTA: initial results *Neuroradiology* **55**(7), 813–818.

Ritschl L, Bergner F, Fleischmann C & Kachelrieß M 2010 Improved sparsity-constrained image reconstruction applied to clinical CT data *in* 'Proceedings of the IEEE Nuclear Science Symposium and Medical Imaging Conference (NSS/MIC) 2010' pp. 3231–3240.

Ritschl L, Bergner F, Fleischmann C & Kachelrieß M 2011 Improved total variation-based CT image reconstruction applied to clinical data *Phys Med Biol* **56**(6), 1545–1562.

Schäfer D, Borgert J, Rasche V & Grass M 2006 Motion-compensated and gated cone beam filtered back-projection for 3-D rotational X-Ray angiography *IEEE Trans Med Imaging* **25**(7), 898–906.

Schultz C, Van Mieghem M, van der Boon R, Dharampal A S, Lauritsch G, Rossi A, Moelker A, Krestin G, van Geuns R, de Feijter P, Serruys P & de Jaegere P 2013 Effect of body mass index on the image quality of rotational angiography without rapid pacing for planning of transcatheter aortic valve implantation: a comparison with multislice computed tomography *Eur Heart J Cardiovasc Imaging* **15**(2), 133–141.

Schwemmer C, Prümmer M, Daum V & Hornegger J 2010 High-density object removal from projection images using low-frequency-based object masking *in* T Deserno, H Handels, H Meinzer & T Tolxdorff, eds, 'Bildverarbeitung für die Medizin 2010 - Algorithmen - Systeme

- Anwendungen' Springer Berlin / Heidelberg pp. 365–369.

Segars W, Mahesh M, Beck T, Frey E & Tsui B 2008 Realistic CT simulation using the 4D XCAT phantom *Med Phys* **35**(8), 3800–3808.

Sotiras A, Davatzikos C & Paragios N 2013 Deformable medical image registration: A survey *IEEE Trans Med Imaging* **32**(7), 1153–1190.

Theriault-Lauzier P, Tang J & Chen G H 2012 Prior image constrained compressed sensing: Implementation and performance evaluation *Med Phys* **39**(1), 66–80.

Thèriault-Lauzier P, Tang J & Chen G H 2012 Time-resolved cardiac interventional cone-beam CT reconstruction from fully truncated projections using the prior image constrained compressed sensing (PICCS) algorithm *Phys Med Biol* **57**(9), 2461–2476.

Tomasi C 1998 Bilateral filtering for gray and color images *in* 'Proceedings of the IEEE International Conference on Computer Vision (ICCV)' pp. 839–846.

van Stevendaal U, von Berg J & Grass M 2008 A motion-compensated scheme for helical cone-beam reconstruction in cardiac ct angiography *Med Phys* **35**(7), 3239–3251.

Wang Z & Bovik A 2002 A universal image quality index *IEEE Signal Proc Let* **9**(3), 81–84.

Wielandts J Y, De Buck S, Ector J, Nuyens D, Maes F & Heidbuchel H 2014 Registration-based filtering: An acceptable tool for noise reduction in left ventricular dynamic rotational angiography images? *in* 'Proceedings of SPIE Medical Imaging 2014: Physics of Medical Imaging' pp. 9036–80.